

SERS in PAH-Os and gold nanoparticle self-assembled multilayers

N. Tognalli, A. Fainstein, E. Calvo, C. Bonazzola, L. Pietrasanta, M. Campoy-Quiles, and P. Etchegoin

Citation: *The Journal of Chemical Physics* **123**, 044707 (2005); doi: 10.1063/1.1954707

View online: <http://dx.doi.org/10.1063/1.1954707>

View Table of Contents: <http://scitation.aip.org/content/aip/journal/jcp/123/4?ver=pdfcov>

Published by the [AIP Publishing](#)

Articles you may be interested in

[Fabrication of quantum dots using multicoated self-assembled monolayer](#)

J. Vac. Sci. Technol. A **28**, 730 (2010); 10.1116/1.3360923

[Detection of electrical characteristics of DNA strands immobilized on self-assembled multilayer gold nanoparticles](#)

Appl. Phys. Lett. **89**, 203902 (2006); 10.1063/1.2390653

[Surface enhanced Raman scattering of p -aminothiophenol self-assembled monolayers in sandwich structure fabricated on glass](#)

J. Chem. Phys. **124**, 074709 (2006); 10.1063/1.2172591

[Resonant Raman spectroscopy of PAH-Os self-assembled multilayers](#)

J. Chem. Phys. **120**, 1905 (2004); 10.1063/1.1635806

[Self-assembled gradient nanoparticle-polymer multilayers investigated by an advanced characterization method: microbeam grazing incidence x-ray scattering](#)

Appl. Phys. Lett. **82**, 1935 (2003); 10.1063/1.1563051



SERS in PAH-Os and gold nanoparticle self-assembled multilayers

N. Tognalli^{a)} and A. Fainstein

Centro Atómico Bariloche and Instituto Balseiro, Comisión Nacional de Energía Atómica, 8400 San Carlos de Bariloche, Río Negro, Argentina

E. Calvo and C. Bonazzola

Instituto de Química Física de los Materiales, Medio Ambiente y Energía (INQUIMAE)-Facultad de Ciencias Exactas y Naturales, Universidad de Buenos Aires, Pabellón 2, Ciudad Universitaria, AR-1428, Buenos Aires, Argentina

L. Pietrasanta

Centro de Microscopías Avanzadas-Facultad de Ciencias Exactas y Naturales, Universidad de Buenos Aires, Pabellón 1, Ciudad Universitaria, AR-1428, Buenos Aires, Argentina

M. Campoy-Quiles

The Blackett Laboratory, Imperial College of Science Technology and Medicine, Prince Consort Road, SW7 2BW London, United Kingdom

P. Etchegoin

School of Chemical and Physical Sciences, Victoria University of Wellington, P.O. Box 600, Wellington, New Zealand

(Received 2 November 2004; accepted 23 May 2005; published online 3 August 2005)

We present a detailed structural and surface-enhanced Raman scattering (SERS) study of poly(allylamine) modified with Os(byp)₂CIPyCHO (PAH-Os) and gold nanoparticles self-assembled multilayers [PAH-Os+(Au-nanoparticles/PAH-Os)_n, n=1 and 5]. Atomic force microscopy and variable-angle spectroscopic ellipsometry measurements indicate that the first nanoparticle layer grows homogeneously by partially covering the substrate without clustering. Analyzing the sample thickness and roughness we infer that the growth process advances thereafter by filling with nanoparticles the interstitial spaces between the previously adsorbed nanoparticles. After five immersion steps the multilayers reach a more compact structure. The interaction between plasmons of near-gold nanoparticles provides a new optical absorption around 650 nm which, in addition, allows a more effective SERS process in that spectral region than at the single-plasmon resonance (~530 nm). We compare the electronic resonance Raman and SERS amplification mechanisms in these self-assembled multilayers analyzing Raman resonance scans and Raman intensity micromaps. As a function of nanoparticle coverage we observe large changes in the Raman intensity scans, with maxima that shift from the electronic transitions, to the plasmon resonance, and finally to the coupled-plasmon absorption. The Raman micromaps, on the other hand, evidence huge intensity inhomogeneities which we relate to "hot spots." Numerical discrete dipole approximation calculations including the interaction between gold nanoparticles are presented, providing a qualitative model for the coupled-plasmon absorption and redshifted Raman hot spots in these samples. © 2005 American Institute of Physics. [DOI: 10.1063/1.1954707]

I. MOTIVATION

The assembly of nanocrystals with a narrow size distribution in two- and three-dimensional arrays has become an important issue in developing nanoparticle-based advanced electronic, optical, and sensing devices.^{1,2} Since the pioneering work of Brust *et al.*³ gold nanoclusters covered with self-assembled monolayers (SAMs) have shown unique size-dependent optical, electronic, magnetic, transport, and mechanical properties due to discrete quantized energy-level spectra. The layer-by-layer (LbL) electrostatic adsorption deposition has become the preferred technique used to generate these self-assembled films due to a series of fundamental advantages:⁴ (i) The different component (polymer, enzyme,

or nanoparticle) concentrations can be better quantified during the deposition process, (ii) a well-defined spatial distribution of the components can be achieved and mass transport limitations can be minimized in nanometer-scale ultrathin films, (iii) the subnanometric geometry control also allows to generate a more directional and effective electronic transport than in disorder structures, and (iv) the self-assembled layer interdiffusion makes possible a true molecular wiring. Hodak *et al.*⁵ introduced redox enzymes deposited with a polycationic redox mediator in ordered multilayers using this technique and the redox mediation of glucose oxidase in self-assembled structures formed with the enzyme and poly(allylamine) modified with Os(byp)₂CIPyCHO (PAH-Os) has been studied.^{6,7} The assembly of derivatized gold nanoparticles with polyelectrolyte self-assembled multilayers has

^{a)}Electronic mail: tognalli@cab.cnea.gov.ar

been studied by Song *et al.*,⁸ in particular as regard the directional electron transport. The incorporation of biomolecules with direct electrical contact to nanoparticles has been introduced by Xiao *et al.* by wiring glucose oxidase to Au nanoparticles.⁹ Different techniques have been applied for the study of these self-assembled nanostructures, including ellipsometry,⁷ quartz-crystal microbalance,⁷ electroacoustic admittance in thickness shear mode resonators,⁶ cyclic voltammetry,¹⁰ and infrared reflection-absorption spectroscopy.¹¹ In a previous work we have studied the vibrational and electronic structure of PAH-Os self-assembled multilayers with Raman spectroscopy and *in situ* electrochemistry.¹²

The power of the Raman technique relies on its high chemical specificity. Unfortunately, Raman cross sections are typically small. To surmount this limitation, signal amplification mechanisms are typically used. One path for Raman amplification referred to as resonant Raman scattering (RRS) is based on electronic resonance enhancement.¹³ This process involves the tuning of the energies of the incident and/or scattered photons with a particular electronic transition of the system under study. This mechanism leads typically to cross-section enhancement factors around 10^5 but the amplified vibrational peaks only belong to a reduced set composed by those excitations that interact with the electronic level involved in the resonance. An alternative amplification process is surface-enhanced Raman scattering (SERS). This extensively used technique relies in the use of metallic rough surfaces, tips, or particles, with nanometric characteristic sizes.¹⁴ The main contribution to the effect is caused by the enhancement of the electromagnetic field in the proximity of the metallic structures due to the excitation of surface plasmons.^{15,16} This enhancement is responsible for the reported 10^{14} Raman cross-section amplification which allows single-molecule Raman spectroscopy.¹⁷⁻¹⁹ The use of gold nanoparticles as a building block to get a SERS amplification in organic multilayers has several potential benefits: it may lead to SERS-active substrates that are characterizable at both the macroscopic and the microscopic level, highly reproducible, simple to prepare in large numbers, and with roughness tunable by the colloid diameter and the average interparticle spacing. In addition, it may help to improve the wiring mechanism inside the film. Self-assembled multilayers of gold nanoparticles and organic thin films combine the advantages of the LbL technique to generate electrochemical wired systems and the chemical specificity and amplification of SERS to study them.

We present a comprehensive study of PAH-Os and gold nanoparticle self-assembled multilayers, relating the structural and optical properties of these films with their SERS response. In particular we analyze the growth, structural assembly, and homogeneity of these films using atomic force microscopy (AFM) images and variable-angle spectroscopic ellipsometry (VASE). The nanoparticle interaction, the plasmon behavior, and their effect over SERS are studied using VASE, optical absorption, and intensity Raman profile measurements. Through resonant Raman scans and Raman intensity micromaps we analyze the resonance mechanisms and the spatial localization of the SERS effect

in these multilayers. Finally, we present discrete dipole approximation (DDA) calculations²⁰⁻²² that model the interaction between gold nanoparticles, providing a qualitative description of the experimental results.

The paper is organized as follows. In Sec. II we describe the sample fabrication procedure and we present the different experimental setups used. Section III contains the experimental results and discussion, while Sec. IV presents the numerical model and results for the interacting nanoparticle arrays. Finally, some conclusions are presented in Sec V.

II. SAMPLES AND EXPERIMENTAL SETUP

The samples were prepared following procedures detailed in previous publications.^{7,11,23} The substrates consist of gold films (~ 150 nm thick) evaporated on Si(001) wafers. The adsorption time for each component, thiol, polymer, and gold nanoparticles were determined by a preliminary quartz-crystal microbalance study.²⁴ The fresh gold film substrate was, first of all, modified with sulfonate groups by immersion in a 3-mercaptopropanesulfonic acid sodium salt (MPS) solution for 2 h, followed by rinsing with de-ionized water. The first polycation layer was formed on the thiol-modified Au substrate by immersion in a PAH-Os aqueous solution for 10 min. The next and subsequent layers were deposited onto the modified surface by alternate immersion in a gold nanoparticle aqueous colloid (nano-Au), then on a polycation solution, and so on, every step lasting again 10 min. Each step was completed by thoroughly rinsing with distilled water and drying. The LbL sequential immersion and rinsing process was carried out using an automatic Microm DS 50 programmable slide stainer from Zeiss, Inc. adapted for the present samples. In this manner LbL supramolecular structures of nominal PAH-Os+(nano-Au/PAH-Os)_n ($n=1,5$) were built by reverting the surface charge of the topmost layer. In this work we study four different samples: S1 and S2 are PAH-Os+(nano-Au/PAH-Os)_n multilayers with $n=1$ and 5, respectively, both grown using 20-nm gold nanoparticles. S3 is a PAH-Os+(nano-Au/PAH-Os)₁ multilayer assembled with bigger gold nanoparticles (~ 50 nm) which evidenced a high degree of clustering during the fabrication process. Colloidal gold was prepared following the procedure reported by Griffin Freeman *et al.* by reduction of HAuCl₄ with citrate and particle size was verified by transmission electron microscopy (TEM) and light scattering as reported elsewhere.²⁵ Finally, S4 is a reference PAH-Os+(PVS/PAH-Os)₅ film, without gold nanoparticles, used for comparison purposes. Here PVS means poly(vinyl)sulphonate.

Tapping-mode AFM was performed in dry nitrogen using a Nanoscope III multimode AFM (Digital Instruments, Veeco Metrology, Santa Barbara, CA) with a *J*-type piezoelectric scanner having a maximal lateral range of 150 μm . Microfabricated silicon cantilevers 125 μm in length and a force constant of ~ 40 N m⁻¹ were used. The cantilever oscillation frequency was tuned to the resonance frequency (280–350 kHz). After a period of 15–30 min of thermal relaxation, initial engagement of the tip was achieved at a scan size of zero to minimize sample deformation and tip con-

tamination. The 512×512 -pixel images were captured with a scan size between 0.5 and 5 μm at a scan rate of 1–2 scan lines/s. Images were processed by flattening using the NANOSCOPE software (Digital Instruments) to remove the background slope. Height, full width at half maximum (FWHM), and roughness were measured with the NANOSCOPE software. In the analysis of nanoparticle diameters, the FWHM measurements were used as a first-order compensation for the systematic distortions introduced by the convolution between the conical tip geometry and the sample profile.

Optical transmission experiments were performed at room temperature using a double-beam UV-Vis Shimadzu UV-1606 spectrophotometer. Experiments will be reported for the PAH-Os modified polymer and the gold colloid both in water solution. VASE was carried out at room temperature using a SOPRA rotating polarizer ellipsometer. The incident angle was varied from 55° to 75° in 2° steps, across a wavelength range from 315 to 850 nm every 2 nm. The optical constants were deduced by numerical inversion of the ellipsometry data using the Levenberg–Marquard algorithm.

The resonant Raman scan experiments were performed using a Jobin–Yvon T64000 triple spectrometer operating in subtractive mode and equipped with a liquid- N_2 -cooled charge-coupled device (CCD). The excitation was done using energies between 1.51 eV (821 nm) and 1.739 eV (713 nm) from a Ti-sapphire solid-state laser, 1.962 eV (632 nm) from a He–Ne ion laser, and energies between 1.834 eV (673 nm) and 2.707 eV (458 nm) from the 17 lines of an Ar–Kr ion laser. Typical powers were around 20 mW, concentrated on a ~ 7 -mm-long and ~ 100 - μm -wide line focus. This line focus was chosen to reduce the photon-induced degradation of the samples. To avoid accumulating this effect a fresh spot in the sample was used after taking each spectra. For the resonant Raman scans the Raman intensity was corrected for the setup response (gratings plus CCD).

Raman micromaps were acquired using a Renishaw 2000 Ramascope single spectrometer, equipped with a peltier cooled CCD and coupled to an Olympus BH-2 confocal microscope with a mapping stage controlled by the acquisition software. The excitation was done using the 1.962-eV (632-nm) line from a He–Ne ion laser. In this case the power was 1 mW, concentrated on a *circular* focus of ~ 1 - μm diameter with an Olympus MDPlan 100 \times , 0.95 numerical aperture microscope objective.

III. RESULTS AND DISCUSSION

A. Structural characterization

The structural characterization of the samples was accomplished through three different quantities obtained from AFM and ellipsometry: (i) roughness, derived from AFM height profiles, (ii) characteristic length, an AFM derived quantity which averages the diameters of both clusters and isolated nanoparticles, and (iii) film thickness, calculated from VASE measurements.²⁶

In Fig. 1 we compare the AFM images of multilayers S1 and S2. We identify the bright quasispherical dots with gold nanoparticles while the background, in a darker gray scale, corresponds to the grains of the gold film evaporated over

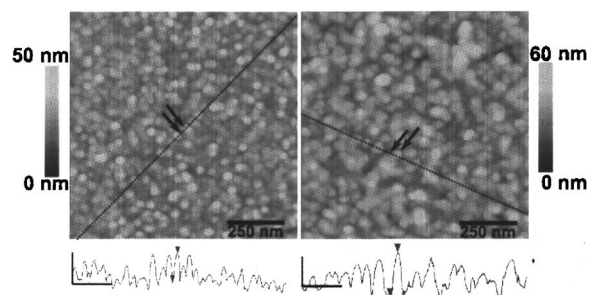


FIG. 1. AFM images of PAH-Os+(nano-Au/PAH-Os)₁ and PAH-Os+(nano-Au/PAH-Os)₅ multilayers, on the left and right, respectively, measured in a $1\text{-}\mu\text{m}^2$ area. The dotted lines indicate the linear regions where the section analysis shown at the bottom of each figure was performed. The arrows indicate particular nanoparticle profiles. In the bottom curves the vertical axes represent a 20-nm scale while the horizontal axes correspond to a 250-nm scale.

the Si substrate. At the bottom of both AFM images we show typical height profiles measured in the linear regions indicated with dotted lines. We analyze 20 random selected profiles from each sample in order to achieve reliable values for roughness and characteristic length. By analyzing carefully the images and the profiles it is possible to identify a majority of isolated nanoparticles in S1 (left image) and to distinguish between isolated nanoparticles and clusters of two or three gold particles in S2 (right image). In S1 we find that the average *background* roughness is 7.7 ± 0.9 nm and its characteristic grain length is 33.8 ± 4.1 nm. The 20-nm diameter nanoparticles are homogeneously distributed over the substrate partially covering the surface. The full sample roughness is 16.4 ± 3.7 nm, a value that results smaller than the nanoparticle diameter because the roughness calculation averages substrate areas with and without nanoparticles. There also exists a reduced number of clusters formed by no more than two nanoparticles, approximately $15/\mu\text{m}^2$. This can be seen in the measured characteristic length, 26.2 ± 2.6 nm, which taking into account these clusters and isolated nanoparticles reaches a value which is just a little larger than the nanoparticle diameter. Using the VASE technique we obtained 15.2 ± 0.5 nm for the film thickness of S1²⁷ in agreement with the measured roughness and a partial coverage. We can conclude that the gold colloid adsorption during the sample fabrication is efficient to reach a homogeneous well-defined 20-nm gold nanoparticle layer but the coverage is not complete.

As can be derived from the AFM image of S2 (right panel in Fig. 1), the multilayer morphology has changed in comparison with S1. We can distinguish a lower density of isolated quasispherical nanoparticles while the clusters of two and more nanoparticles appear more frequently as irregular-shaped spots. This becomes evident also by the increase in the characteristics length to 41.6 ± 9 nm, a value which is close to the characteristic size of a two-particle cluster. The average roughness, on the other hand, increases only slightly to 18.2 ± 4 nm, a value close to the 20-nm characteristic nanoparticle diameter. The sample thickness obtained from ellipsometry measurements, 29.8 ± 0.5 nm, almost duplicates that derived for S1. Considering that this technique probes the whole film, the roughness of S2 can be

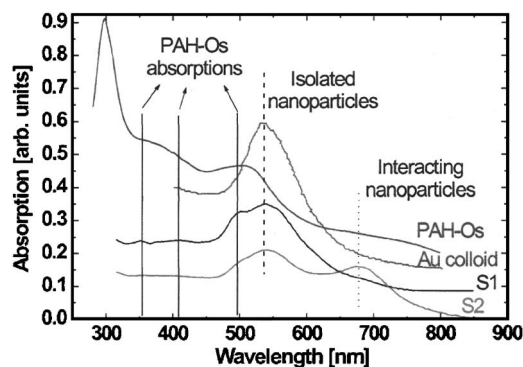


FIG. 2. Optical-absorption spectra for PAH-Os and 20-nm Au colloid, both measured through optical transmission in aqueous solution, and optical-absorption spectral for PAH-Os+(nano-Au/PAH-Os)₁ (S1) and PAH-Os+(nano-Au/PAH-Os)₅ (S2) multilayers, both measured using VASE. We indicate the PAH-Os characteristic absorption with vertical full lines, while the plasmon absorptions related to isolated and interacting nanoparticles are indicated by vertical dashed and dotted lines, respectively.

understood as due to the AFM tip measuring only a second nanoparticle layer that lies over a compact background of nanoparticles. Within this picture, the growth evolves with nanoparticles filling the empty spaces until a full layer is completed, and only two layers are formed after five steps of gold colloid immersion.

We also characterized the multilayers through their optical response. In Fig. 2 we show the optical absorption spectra of PAH-Os and a 20-nm Au colloid, both in aqueous solution, and we compare them with the optical absorption of S1 and S2 measured using VASE. In the PAH-Os absorption spectrum we can identify three main absorptions: (i) one intense around 300 nm and related to deep electronic transitions, (ii) a weaker line centered at ~ 375 nm, and (iii) the metal to ligand charge-transfer (MLCT) transition around 500 nm. We have exploited the MLCT transition in Ref. 12 for resonance Raman-scattering amplification to measure *in situ* electrochemical processes in self-assembled multilayers. The gold colloid spectrum, on the other hand, presents a broad and very intense absorption around 530 nm associated with the 20-nm gold nanoparticle plasmon mode. The absorption spectrum of S1 shows the presence of both PAH-Os and gold nanoparticles in the single monolayer through their respective characteristic peaks. The more intense peak belongs to the nanoparticle plasmon and it is centered at ~ 530 nm. Mounted on this peak appears the PAH-Os MLCT transition at ~ 500 nm. The absorption spectra of PAH-Os and gold nanoparticles are similar in aqueous solution and in this self-assembled multilayer. Note, however, that the broad PAH-Os peak around ~ 375 nm present in solution seems to split into two distinguishable absorptions in the self-assembled structure. Finally, the absorption spectrum of S2 presents all the same peaks that appear for S1 plus an extra redshifted absorption at ~ 680 nm.²⁵ Based on a previous work this latter feature is assigned to interacting gold nanoparticle plasmons.²¹ Its presence is compatible with the increased amount of gold nanoparticle clusters and the more compact structure observed and discussed through the above-presented AFM images. These results show the high sensitivity of the VASE technique in ultrathin multilayers.

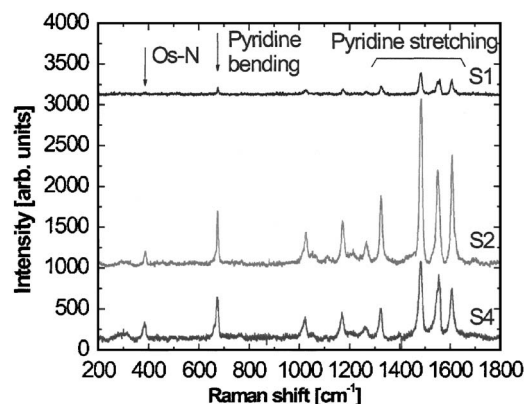


FIG. 3. Raman spectra of samples S1, S2, and S4 measured using the 514.5-nm Ar-Kr laser line. The most intense peaks belong to the pyridine stretching ($1325\text{--}1606\text{ cm}^{-1}$), pyridine bending (670 cm^{-1}), and Os vibration (383 cm^{-1}), all resonant with the PAH-Os MLCT transition.

B. Resonant Raman scattering

From the structural and optical characterization we conclude that (i) S1 is homogeneously but partially covered by isolated nanoparticles, while two layers and nanoparticle clustering can be identified in S2, and (ii) three main optical-absorption lines characterize the samples, related to a MLCT transition (~ 500 nm), the plasmon resonance (~ 530 nm), and a coupled-plasmon mode (~ 680 nm). In this section we will discuss how these features affect the Raman resonances in these multilayers. We recall that the laser spot used for the resonance Raman scans has a linear shape of $7\text{ mm} \times 100\text{ }\mu\text{m}$. This large area averages the Raman signal from different local polymer and nanoparticle environments. We begin introducing in Fig. 3 the Raman spectra of samples S1, S2, and S4 measured using the 514.5-nm Ar-Kr laser line. The three spectra have basically the same shape but they differ in intensity. The most intense peaks belong to the pyridine stretching ($1325\text{--}1606\text{ cm}^{-1}$), pyridine bending (670 cm^{-1}), and Os-N vibration (383 cm^{-1}), all spatially related to the electronic levels involved in the PAH-Os MLCT transition. We find that in these measurements we cannot distinguish the vibrations belonging to the polymer backbone. In a previous work we found that the Raman intensity of (PVS/PAH-Os) multilayers scales with the number of PAH-Os layers.¹² This relation is not maintained when Au nanoparticles are present. In fact, note that the S2 [PAH-Os+(nano-Au/PAH-Os)₅] Raman intensity is five times larger than that of S1, though in principle it has three times more polymer deposition cycles. Moreover, it has more than two times larger intensity than that of S4 [PAH-Os+(PVS/PAH-Os)₅], even when both samples have equal number of deposition cycles. The main conclusions derived from Fig. 3 are (i) the Raman spectra evidence that the molecular structure is preserved in the PAH-Os+(nano-Au/PAH-Os)_n multilayers, and (ii) using as excitation the 514.5-nm line, the enhancement selectivity of the PAH-Os MLCT transition resonance prevails over the gold nanoparticle plasmon resonance. Assuming equal deposited PAH-Os mass in S2 and S4, we conclude that at 514.5 nm the assembled gold nanoparticles only produce an average enhancement factor of ~ 2 over the Raman signal.

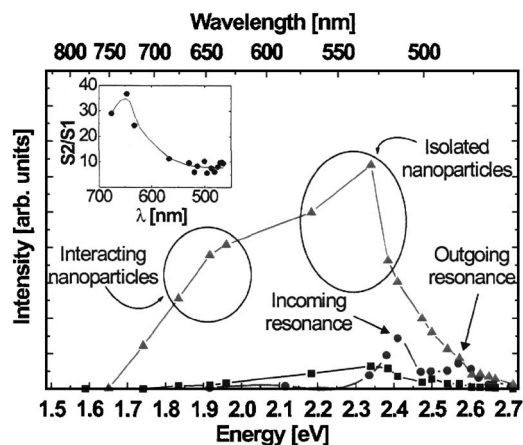


FIG. 4. Raman resonance profiles of PAH-Os+(PVS/PAH-Os)₅ (full circles), PAH-Os+(nano-Au/PAH-Os)₁ (full squares), and PAH-Os+(nano-Au/PAH-Os)₅ (full triangles) multilayers. We indicate with arrows the incoming and outgoing electronic Raman resonances on the PAH-Os+(PVS/PAH-Os)₅ multilayer. SERS amplification regions related to isolated and interacting nanoparticles are indicated with circles. The inset shows the Raman intensity ratio between samples 2 and 1 for different wavelengths.

In order to deepen the analysis of the resonance response of the different multilayers we present in Fig. 4 the Raman intensity of the 1483 cm^{-1} peak as a function of laser energy measured on S1 (full squares), S2 (full triangles), and S4 (full circles). We start analyzing the multilayer without gold nanoparticles, S4. We identify two intensity maxima related to the incoming and outgoing electronic Raman resonances.¹² The first peak, situated around 515 nm, is due to the energy tuning between the incident photon and the PAH-Os MLCT transition. The second appears blueshifted $\sim 1483\text{ cm}^{-1}$ with respect to the MLCT transition because for the outgoing resonance it is the scattered photon that resonates with the MLCT transition.¹² If we look at the resonance profiles of S1 and S2, the samples with gold nanoparticles, we observe instead only one peak centered at 530 nm, exactly at the plasmon energy. This means that the electronic resonance is shadowed by the SERS effect. Note, however, that incoming and outgoing resonances by the plasmon mode could in principle exist but cannot be separated due to the relatively broad related absorption (see Fig. 2). Particularly notorious are the results of S2 where the resonance maximum (at $\sim 530\text{ nm}$) is only 12 times greater than the Raman intensity of S4 at the same wavelength, which has nominally the same PAH-Os adsorbed mass but no gold nanoparticles. This means that the presence of nanoparticles produces a small increase of the intensity at the plasmon energy as compared with typical SERS performances.^{17–19} This poor amplification factor is probably related to the signal average of highly diluted SERS active sites inside the 0.7-mm^2 spot.

Note that for S2 in Fig. 4, besides the shift of the PAH-Os MLCT electronic transition to the gold nanoparticle plasmon resonance, a shoulder appears around $\sim 650\text{ nm}$ in the resonance profile. In view of the fact that, as derived from AFM and VASE measurements S2 has a more compact structure, and that this feature is spectrally coincident with the optical-absorption peak observed at 670 nm in Fig. 2, it is straightforward to associate the increased scattering with

the SERS amplification mechanism created by the interacting gold nanoparticle plasmons.²¹ To further illustrate this point we show in the inset of Fig. 4 the Raman intensity ratio between samples 2 and 1. There are two important things to note. First, the SERS amplification due to isolated nanoparticles (around 530 nm) is more efficient in sample 2 because the signal is ten times greater when the nominal PAH-Os mass deposition is only three times larger. This is related to an improvement in the SERS efficiency due to the subsequent adsorption of PAH-Os and gold nanoparticles (note that five immersion cycles result in an ~ 2 -layer self-assembled gold nanoparticle film). Second, the SERS amplification due to interacting nanoparticles (around 650 nm) is 40 times larger in sample 2 because of the compact structure formed inside the two nanoparticle layers and the presence of an increased number of gold nanoparticles clusters. It is worth to mention that this mechanism is believed to be responsible for the so called “hot spots,” very intense SERS amplification areas with gain factors of $\sim 10^{14}$ which make possible single-molecule Raman spectroscopy.^{17–19} The main conclusions derived from the previous analysis can then be summarized as follows: (i) the multiple adsorption of PAH-Os and gold nanoparticles needed to complete each layer increase the SERS efficiency, and (ii) the more compact structure presents a higher interaction between nanoparticle plasmons which is reflected in the $\sim 650\text{-nm}$ region through the appearances of a new optical absorption, a shoulder in the Raman intensity profile, and a maximum in the Raman amplification ratio between samples 2 and 1.

C. Micro-Raman maps

To gain further insight on the SERS effect in these self-assembled multilayers we performed micro-Raman maps of samples S1, S2, and of another optimized sample, S3, which has a higher proportion of homogeneously distributed gold nanoparticle clusters (around $40/\mu\text{m}^2$). The results are qualitatively similar in all three samples, but the main characteristics we want to highlight were clearer in S3. Thus we will concentrate our analysis in this latter sample.

In Fig. 5 we compare some of the 120 SERS spectra sequentially measured every $1\ \mu\text{m}$ inside a $10 \times 10\text{-}\mu\text{m}^2$ region on S3 (spectra 2–9) using the 632-nm He–Ne laser and a $1\text{-}\mu\text{m}^2$ spot, with an electronic resonant Raman spectrum (number 1) measured on S4 using the large line focus of the 514.5-nm Ar–Kr laser line. The vertical dotted lines indicate the peak positions characteristic of PAH-Os observed in spectrum 1. These peaks correspond, as we have mentioned before, to the Os center and ligand-related vibrational modes and their selective enhancement is caused by the electronic Raman resonance tuned to the PAH-Os MLCT transition.^{12,28–32} Spectra 2–9 are qualitatively different from the previous one. First, the Os and ligand-related lines appear but with different relative intensities, specially in the pyridine stretching region ($1325\text{--}1606\text{ cm}^{-1}$). In addition, some of the lines are somewhat shifted, around 3 cm^{-1} . Second, the spectra also show a series of new well-defined peaks. We have assigned the new features by comparison with Raman signals from similar compounds as Os(bpy)₃²⁺ or

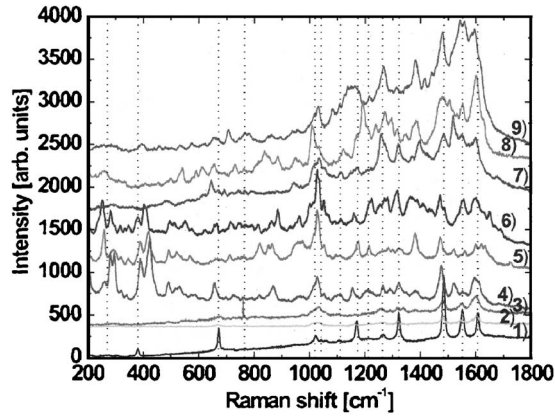


FIG. 5. Raman spectrum of the PAH-Os+(PVS/PAH-Os)₅ multilayer (spectrum 1), taken under electronic Raman resonance with the PAH-Os MLCT transition. Spectra 2–9 correspond to different SERS measurements on a PAH-Os+(nano-Au/PAH-Os)₁ multilayer that displayed nanoparticle clustering (S3) using the 632.8-nm He–Ne laser line with a $\sim 1\text{-}\mu\text{m}^2$ spot inside a $100\text{-}\mu\text{m}^2$ area. The dotted lines indicate the Os center and ligand-related modes. Most of the new peaks that appear on spectra 2, 3, and 7–9 are related to the polymer backbone while the more intense peaks in the 200–500- cm^{-1} region correspond to a pyridine selective enhancement.

Os(bpy)₂(P²⁺)²⁺ (Ref. 31) and other functional groups similar to the ones present in PAH-Os, e.g., pyridines, bipyridines, polystyrenes, disubstituted benzenes, and polyethenes.³³ We find that some of the new signals appearing in spectra 2, 3, and 7–9 (~ 710 , ~ 1080 , ~ 1295 , and $\sim 1410\text{ cm}^{-1}$) can be identified with the polymer backbone vibrations. Spectra 4–6 merit special consideration because of their similar behavior. In contrast to the other spectra, we observe a selective amplification of several peaks centered at ~ 250 , ~ 290 , ~ 390 , ~ 420 , ~ 1020 , and $\sim 1040\text{ cm}^{-1}$. These signals come from pyridine, implying that this selective amplification reflects its proximity with a hot spot.

To illustrate the spatial distribution of the SERS effect we show in Fig. 6 a Raman intensity micromap corresponding to spectra taken on S3 with the 632-nm laser line every $1\text{ }\mu\text{m}$ and with a submicron spot size. The shape of all the

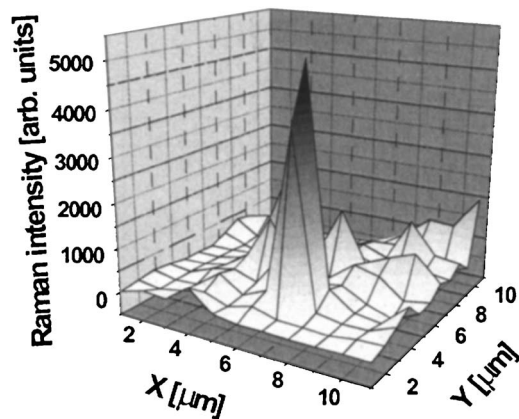


FIG. 6. Raman micromap where the z axis represents the values of the integrated area below the spectral region involving the 1483- and 1606- cm^{-1} peaks (bipyridines) without the background contribution. Spectra were taken every $1\text{ }\mu\text{m}$ with a $\sim 1\text{-}\mu\text{m}^2$ spot size. A very localized region can be observed under the effects of a great amplification. The intensity value is 10^3 times larger than the less-amplified regions and two orders of magnitude bigger than the background average.

spectra reflects the existence of SERS enhancement as displayed in Fig. 5. The shown signal was obtained integrating the Raman lines between 1483 and 1606 cm^{-1} (bipyridine vibrations) and subtracting the background. A very localized region with a peak of more than 5000 units can be clearly observed with FWHM corresponding to the micro-Raman resolution. This signal is two orders of magnitude larger than the average SERS intensity derived from the micromap. This average corresponds to what would be detected with a macro-optics setup. Besides the larger peak, some ~ 16 other relative maxima (from the 120 sampled points) can be identified with intensities at least ten times larger than the average SERS signal. Interestingly, a similar experiment performed with a 514.5-nm laser excitation (i.e., tuned to the *single-plasmon* resonance) displayed a rather uniform Raman intensity map, without localized amplified regions. This strongly indicates that coupled-plasmon resonances (i.e., coupled nanoparticles) are at the origin of the observed spatially inhomogeneous Raman enhancement. We recall that AFM images of this particular sample exhibit some 40 clusters formed by 2–5 gold nanoparticles per μm^2 . Thus, some ~ 5000 clusters are expected to exist in the $11 \times 11\text{-}\mu\text{m}^2$ region sampled by the micromap displayed in Fig. 6. Consequently, the inhomogeneity observed at the micrometer scale, if due to hot-spots with origin in clusters at the nanoscale, implies that only a few of the latter lead to high amplification regions.

IV. NUMERICAL MODEL

A qualitative description of the dielectric response of the self-assembled gold nanoparticle layers can be attained using a DDA model for the interacting nanoparticle plasmons. For this purpose we follow Refs. 20–22 and consider a two-dimensional (2D) colloidal array of N spherical gold nanoparticle of radius R random distributed inside a $L \times L$ area. Each colloid has its own surface-plasmon resonance and interacts with the rest of the particles through a dipole-dipole electromagnetic interaction. As a consequence of this interaction, the induced dipole at each colloid will have a direction and magnitude that can be solved self-consistently as²¹

$$\mathbf{p}_i = \alpha(\nu)\mathbf{E}_i = \alpha(\nu)(\mathbf{E}_0 + \mathbf{E}_i^{\text{dip}}), \quad (1)$$

with

$$\mathbf{E}_i^{\text{dip}} = \sum_{j \neq i} \frac{e^{ikr}}{r^3} [k^2(\mathbf{r}_{ij} \times \mathbf{p}_j) \times \mathbf{r}_{ij} + (1 - ikr)(3\hat{r}_{ij}(\mathbf{p}_j \cdot \hat{r}_{ij}) - \mathbf{p}_j)] \quad (2)$$

and

$$\alpha(\nu) = R^3 \frac{\epsilon_i(\nu) - \epsilon_0}{\epsilon_i(\nu) + 2\epsilon_0}. \quad (3)$$

Here \mathbf{p}_i is the induced dipole moment associated with the colloid at site i , α is the polarizability of a gold nanoparticle, \mathbf{E}_0 is the external electric field with wave vector \mathbf{k} , $\mathbf{E}_i^{\text{dip}}$ is the electric field at colloid i generated by all the other dipoles, \mathbf{r}_{ij} is the position vector between colloid i and j , $r = |\mathbf{r}_{ij}|$, $\hat{r}_{ij} = \mathbf{r}_{ij}/r$, and ϵ_i and ϵ_0 are the dielectric functions

of the nanoparticle metal (Au in this case) and the surrounding medium, respectively. Note that Eq. (2) takes into account both the so-called quasistatic contribution and retardation.^{20,21} For the dielectric function of gold we used the values from Ref. 34. Considering a surrounding medium with $\epsilon_0=1.35$, a value between vacuum and water, $\alpha(\nu)$ displays a resonance at $\lambda_p=511.8$ nm, for which $\epsilon_i(\lambda_p)=-2.7059+i0.7264$. This resonance corresponds to the isolated nanoparticle plasmon excitation, and coincides quite closely with the experimentally determined value of $\sim\lambda_p=530$ nm (see Fig. 2).

To implement the numerical solution of this problem we define a simple square lattice of spacing $d_0=1$ nm inside the $L\times L$ area, with $L=1000$ nm, where we locate N spherical nanoparticles of radius $R=10$ nm at random, avoiding spatial superposition and assigning each individual colloid to an effective total dipole. This last consideration is justified because the nanoparticle size is typically a fraction of the light wavelength. N will depend on the sample that we want to model. \mathbf{E}_0 is set along the \hat{x} direction with wave vector $\mathbf{k}=k\hat{z}$ (\hat{z} here is normal to the self-assembled multilayers). The incident wavelength was set to $\lambda_0=511.8$ nm, that is, coupled to the nanoparticle plasmon resonance. In order to determine the magnitude and orientation of all the dipoles we generate a configuration of random unit dipoles, \mathbf{p}_i , at each colloid and then we iterate using the following procedure: (i) we evaluate the electric field at each nanoparticle produced by all the others using Eq. (2) and (ii) we define a new dipole at \mathbf{r}_i through a modification of Eq. (1),

$$\mathbf{p}_i^{l+1} = \eta\alpha(\nu)\mathbf{E}_i^{l+1} + (1 - \eta)\mathbf{p}_i^l. \quad (4)$$

Here l indicates the iteration step and η is an *ad hoc* parameter to improve convergence which was usually set between 0.5 and 0.1.²² Finally, we repeat these two steps until a stable field configuration is achieved.

With the obtained self-consistent-field configuration, the spatial intensity distribution can be calculated using the relation $I=0.5 \text{Re}\{\mathbf{E}\mathbf{E}^*\}$.³⁵ On the other hand, the energy eigenvalues and eigenvectors for the interacting plasmon problem can be derived from the matrix:²¹

$$U_{ij} = \delta_{ij}\omega_p - (1 - \delta_{ij})\mathbf{p}_i \cdot \frac{e^{ikr}}{r^3} [k^2(\mathbf{r}_{ij} \times \mathbf{p}_j) \times \mathbf{r}_{ij} + (1 - ikr)(3\hat{r}_{ij}(\mathbf{p}_j \cdot \hat{r}_{ij}) - \mathbf{p}_j)]. \quad (5)$$

Here $\omega_p=2\pi c/\lambda_p$ is the surface-plasmon angular frequency for the uncoupled colloid. Following Ref. 21, to characterize the eigenvectors associated with each eigenvalue we associate with the i th colloid with coordinate \mathbf{r}_i a Gaussian with standard deviation σ equal to the radius of the colloid, R . Thus, the spatial representation of the participation of different colloids in a specific eigenvalue is given by the function

$$F^j(\mathbf{r}) = \left| \sum_i a_i(j) e^{-|\mathbf{r} - \mathbf{r}_i|^2/2R^2} \right|^2, \quad (6)$$

where $a_i(j)$ is the i th coefficient (associated with the i th colloid) of the j -eigenvector linked to the j -eigenvalue ω_j .

To illustrate the physics behind the problem of interacting nanoparticles, we first show in Fig. 7 the field distribu-

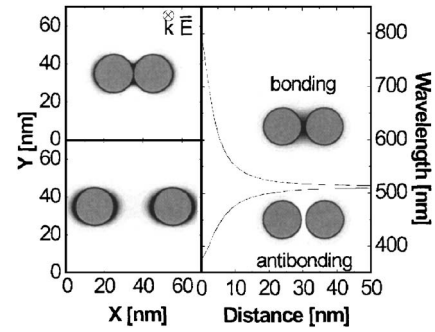


FIG. 7. Field distribution for nanoparticles separated at 0 nm (left-top panel) and 20 nm (left-bottom panel). The laser field is applied along the line connecting the two nanoparticles and the wave vector is perpendicular to the plane of the nanoparticles. The right panel displays the eigenvalues corresponding to the bonding (top line) and antibonding (bottom line) states as a function of the nanoparticle separation. The bonding and antibonding eigenfunctions for a configuration of two nanoparticles separated by 2 nm are schematized in this latter panel.

tion and coupled-plasmon energies and eigenvectors for two interacting dipoles. The laser field is applied along the line connecting the two nanoparticles. In the left panel the field distribution for nanoparticles separated at 0 and 20 nm, respectively, is displayed. Two eigenvectors exist for this simple problem, equivalent to bonding and antibonding states. These and their energies as a function of nanoparticle distance are depicted in the right panel on Fig. 7. A hot spot within this scheme corresponds to the large intensity between nanoparticles corresponding to the bonding state. The energy of the latter is smaller than that of the noninteracting nanoparticle, while that of the antibonding state is blueshifted with respect to the independent plasmon. We note, in addition, that the induced polarization is even (odd) for the bonding (antibonding) state, implying that it couples (does not couple) with an external field with wavelength much larger than the separation between nanoparticles. It should be highlighted that the energies of the plasmon states displayed in Fig. 7 are arbitrary in the sense that they depend on the magnitude of the applied laser field (which defines in a large part the magnitude of the induced polarization and thus of the local field). In fact, we have chosen a value of E_0 such that the range of coupled-plasmon energies covers those observed experimentally (see Fig. 2).

When a random distribution of nanoparticles is considered, as in Fig. 8, the interacting nanoparticle energies cover a broad range of energies. In Fig. 8 we show the eigenvalue histogram for 200 nanoparticles randomly distributed in a $1\text{-}\mu\text{m}^2$ square area, together with the eigenvectors for some specific energies located in the bonding, antibonding, and independent energy regions of the spectra. It is quite clear that all these situations coexist in a given sample, leading to states that involve hot-spot-like coupled pairs, odd-symmetry states that do not interact with light, and isolated resonances, respectively.

Figure 9 shows the energy histogram for different coverages, 200, 400, and 1600 nanoparticles randomly distributed in a $1\text{-}\mu\text{m}^2$ square area (a)–(c), and for a closed-packed ordered distribution of 2500 nanoparticles in the same area (d). The histograms are normalized with respect to the total

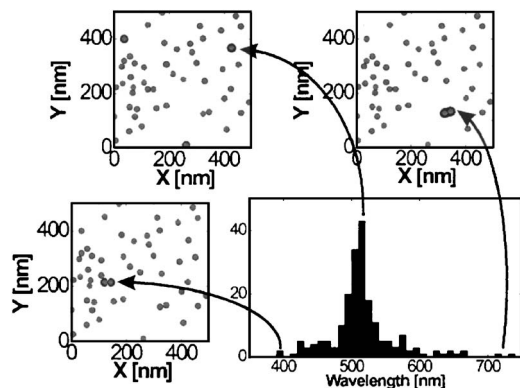


FIG. 8. Eigenvalue histogram for 200 nanoparticles randomly distributed in a $1\text{-}\mu\text{m}^2$ square area (bottom right), together with the eigenvectors for some specific energies located in the bonding (top right), independent (top left), and antibonding (bottom left) energy regions of the spectra.

number of nanoparticles. According to the AFM results, our sample S1 should correspond to a coverage close to (b), and that of S2 to something close to (c). For the lower coverage (a), the spectrum is basically characterized by a peak corresponding to the isolated plasmon resonance ω_p . When the coverage is increased to (b), a peak is still observed centered

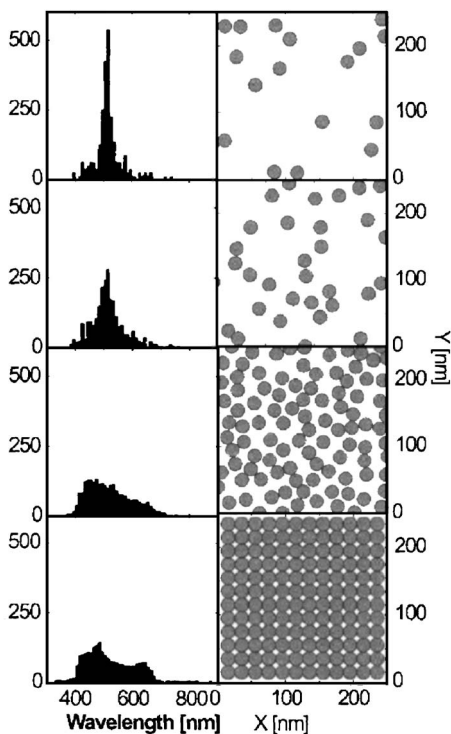


FIG. 9. Energy histogram (left panel) and the respective nanoparticle maps (right panel) for different coverages, 200, 400, and 1600 nanoparticles randomly distributed in a $1\text{-}\mu\text{m}^2$ square area [(a)–(c)], and for a closed-packed ordered distribution of 2500 nanoparticles in the same area (d). The histograms are normalized with respect to the total number of nanoparticles. For the lower coverage (a), the spectrum is basically characterized by a peak corresponding to the isolated plasmon resonance ω_p . When the coverage is increased to (b), a peak is still observed centered at ω_p , but a broadening and low-energy tail clearly develops. When the coverage is further increased to (c), besides the broadening, a peaklike structure arises at longer wavelengths characteristic of the coupled-plasmon resonances. When an ordered structure of nanoparticles is considered (d), the energy histogram has evolved into a bandlike distribution much like what happens with the electronic bands in a crystalline solid.

at ω_p , but a broadening and low-energy tail clearly develops. This agrees qualitatively well with the extinction spectrum of S1 shown in Fig. 2. When the coverage is further increased to (c), besides the described broadening, a peaklike structure arises at longer wavelengths characteristic of the coupled-plasmon resonances. Again, this agrees qualitatively with what is observed for S2 in Fig. 2, where besides the single-plasmon resonance at ~ 530 nm, a second peak appears at ~ 680 nm. According to this simple model, this second absorption can be clearly identified with bondinglike coupled-plasmon states. The latter gives rise to resonant hot spots, which explain the shoulder in the Raman resonance scan of Fig. 4 which is also observed around 650 nm. When an ordered structure of nanoparticles is considered (d), the energy histogram has evolved into a bandlike distribution much like what happens with the electronic bands in a crystalline solid.

V. CONCLUSIONS

We have presented a detailed structural, ellipsometric, and Raman study of self-assembled PAH-Os/Au nanoparticle multilayers. AFM images and VASE thickness measurements indicate that using 20-nm gold colloids the first nanoparticle layer grows homogeneously, partially covering the substrate without nanoparticles clustering. The growth process evolves filling the nanoparticle interstitial spaces and after five immersion cycles inside the same gold colloid only two layers of nanoparticles are self-assembled during the sample fabrication process. The first adsorption of this gold colloid is enough to shift the Raman profile peak related to electronic resonance down to lower energies, evidencing the enhancement in the PAH-Os Raman spectrum due to the electromagnetic plasmon resonance of the gold nanoparticles around 530 nm. The multilayers with five immersion cycles have a more compact structure, presenting an effective plasmon interaction which provides a new optical absorption around 650 nm. This coupled-plasmon absorption leads to a new maximum in the SERS amplification. Raman micro-maps of samples with nanoparticle clustering show the high spatial dilution of hot spots and their great localized amplification. Finally, a DDA numerical model with nanoparticle distribution comparable with that of the studied self-assembled multilayers qualitatively reproduces the appearance of the coupled-plasmon absorption and redshifted hot spots showed by samples with compact colloid structures.

ACKNOWLEDGMENTS

We acknowledge Martin Bellino for help in the sample preparation. Three of the authors (A.F., E.C., and L.P.) are permanent research fellows of CONICET (Argentina).

¹ *Nanoparticles and Nanostructured Films: Preparation, Characterization and Applications*, edited by J. H. Fendler (Wiley-VCH, Weinheim, 1998).

² *Nanoparticle Assemblies*, edited by D. J. Schiffrin (The Royal Society of Chemistry, UK, 2004) [Faraday Discuss. 125, 409 (2004)].

³ M. Brust, M. Walker, D. Bethell, D. J. Schiffrin, R. Whyman, *J. Chem. Soc., Chem. Commun.* **1994**, 801.

⁴ *Multilayer Thin Films*, edited by G. Decher and J. B. Schlenoff (Wiley-VCH, Weinheim, Germany, 2003).

⁵ J. Hodak, R. Etchenique, E. J. Calvo, K. Singhal, and P. N. Bartlett, *Langmuir* **13**, 2716 (1997).

- ⁶E. J. Calvo, E. Forzani, and M. Otero, *Anal. Chem.* **74**, 3281 (2002).
- ⁷E. S. Forzani, M. Otero, M. A. Pérez, M. López Teijelo, and E. J. Calvo, *Langmuir* **18**, 4020 (2002).
- ⁸W. Song, M. Okamura, T. Kondo, and K. Uosaki, *J. Electroanal. Chem.* **554**, 385 (2003).
- ⁹Y. Xiao, F. Pastolsky, E. Katz, J. F. Hinfeld, and I. Willner, *Science* **299**, 1877 (2003).
- ¹⁰E. J. Calvo and A. Wolosiuk, *J. Am. Chem. Soc.* **124**, 8490 (2002).
- ¹¹C. Bonazzola, E. J. Calvo, and F. C. Nart, *Langmuir* **19**, 5279 (2003).
- ¹²N. Tognalli, A. Fainstein, C. Bonazzola, and E. Calvo, *J. Chem. Phys.* **120**, 1905 (2004).
- ¹³For a comprehensive review of resonant Raman scattering see M. Cardona, in *Light Scattering in Solids II*, edited by M. Cardona and G. Güntherodt (Springer, Heidelberg, 1989).
- ¹⁴R. Griffith Freeman *et al.*, *Science* **267**, 1629 (1995).
- ¹⁵M. Moskovits, *Rev. Mod. Phys.* **57**, 783 (1985).
- ¹⁶K. Kneipp, H. Kneipp, I. Itzkan, R. R. Dasari, and M. S. Feld, *J. Phys.: Condens. Matter* **14**, R597 (2002).
- ¹⁷K. Kneipp, Y. Wang, H. Kneipp, L. Perelman, I. Itzkan, R. R. Dasari, and M. S. Feld, *Phys. Rev. Lett.* **78**, 1667 (1997).
- ¹⁸S. Nie and S. R. Emory, *Science* **275**, 1102 (1997).
- ¹⁹R. C. Maher, L. F. Cohen, and P. Etchegoin, *Chem. Phys. Lett.* **352**, 378 (2002).
- ²⁰L. Kelly, E. Coronado, L. L. Zhao, and G. C. Schatz, *J. Phys. Chem. B* **107**, 668 (2003).
- ²¹P. Etchegoin, L. F. Cohen, H. Hartigan, R. J. C. Brown, M. J. T. Milton, and J. C. Gallop, *J. Chem. Phys.* **119**, 5281 (2003).
- ²²E. M. Purcell and C. R. Pennypacker, *Astrophys. J.* **186**, 705 (1973).
- ²³E. J. Calvo, F. Battaglini, C. Danilowicz, A. Wolosiuk, and M. Otero, *Faraday Discuss.* **116**, 47 (2000).
- ²⁴M. Bellino, MSc Physics dissertation, Universidad de Buenos Aires, 2002.
- ²⁵M. G. Bellino, E. J. Calvo, and G. Gordillo, *Phys. Chem. Chem. Phys.* **6**, 424 (2004).
- ²⁶For a detailed description of ellipsometry see R. M. A. Azzam and N. M. Bashara, in *Ellipsometry and Polarized Light* (Elsevier, Amsterdam, The Netherlands, 2003).
- ²⁷A detailed study of thickness measurements of self-assembled multilayers containing Au nanoparticles using ellipsometry will be presented in a future work to be submitted.
- ²⁸A. P. Taylor, J. A. Crayston, and T. J. Dines, *J. Chem. Soc., Faraday Trans.* **93**, 1803 (1997).
- ²⁹D. A. Walsh, T. E. Keyes, C. F. Hogan, and R. J. Forster, *J. Phys. Chem. B* **105**, 2792 (2001).
- ³⁰D. P. Strommen, P. K. Mallick, G. D. Danzer, R. S. Lumpkin, and J. R. Kincaid, *J. Phys. Chem.* **94**, 1357 (1990).
- ³¹J. V. Caspar, T. D. Westmoreland, G. H. Allen, P. G. Bradley, T. J. Meyer, and W. H. Woodruff, *J. Am. Chem. Soc.* **106**, 3492 (1984).
- ³²J. G. Gaudiello, P. G. Bradley, K. A. Norton, W. H. Woodruff, and A. J. Bard, *Inorg. Chem.* **23**, 3 (1984).
- ³³D. Lin-Vien, N. B. Colthup, W. G. Fateley, and J. G. Grasselli, in *The Handbook of Infrared and Raman Characteristic Frequencies of Organic Molecules* (Academic, San Diego, 1991).
- ³⁴D. R. Lide, *Handbook of Chemistry and Physics*, 73rd ed. (CRC, Cleveland, 1992).
- ³⁵A. Yariv, *Optical Electronics*, 4th ed. (Saunders College Publishing, New York, 1971).